PNAS RESEARCH ARTICLE | BIOPHYSICS AND COMPUTATIONAL BIOLOGY

Activation of caspase-9 on the apoptosome as studied by methyl-TROSY NMR

Alexander I. M. Sever[a,b,1], T. Reid Alderson[a,c,d,1,2], Enrico Rennella[a,c,d,2], James M. Aramini[a,c,d], Zi Hao Liu[b,d], Robert W. Harkness[a,b,c,d], and Lewis E. Kay[a,b,c,d,2]

Edited by Peter Wright, Department of Integrative Structural and Computational Biology, Scripps Research Institute, La Jolla, CA; received June 28, 2023; accepted October 23, 2023

Mitochondrial apoptotic signaling cascades lead to the formation of the apoptosome, a 1.1-MDa heptameric protein scaffold that recruits and activates the caspase-9 protease. Once activated, caspase-9 cleaves and activates downstream effector caspases, triggering the onset of cell death through caspase-mediated proteolysis of cellular proteins. Failure to activate caspase-9 enables the evasion of programmed cell death, which occurs in various forms of cancer. Despite the critical apoptotic function of caspase-9, the structural mechanism by which it is activated on the apoptosome has remained elusive. Here, we used a combination of methyl-transverse relaxation-optimized NMR spectroscopy, protein engineering, and biochemical assays to study the activation of caspase-9 bound to the apoptosome. In the absence of peptide substrate, we observed that both caspase-9 and its isolated protease domain (PD) only very weakly dimerize with dissociation constants in the millimolar range. Methyl-NMR spectra of isotope-labeled caspase-9, within the 1.3-MDa native apoptosome complex or an engineered 480-kDa apoptosome mimic, reveal that the caspase-9 PD remains monomeric after recruitment to the scaffold. Binding to the apoptosome, therefore, organizes caspase-9 PDs so that they can rapidly and extensively dimerize only when substrate is present, providing an important layer in the regulation of caspase-9 activation. Our work highlights the unique role of NMR spectroscopy to structurally characterize protein domains that are flexibly tethered to large scaffolds, even in cases where the molecular targets are in excess of 1 MDa, as in the present example.

apoptosis | caspase-9 | protease | NMR spectroscopy | oligomerization

Apoptosis, commonly referred to as programmed cell death, is a biochemical signaling cascade that eliminates targeted or damaged cells. Critical to the development and survival of multicellular organisms, apoptosis not only mitigates aberrant cell growth but also promotes healthy cell turnover in tissues and organs (1–3). Further, apoptosis maintains cellular homeostasis, with as many as 100 billion cells undergoing apoptosis daily in an adult human (4). As a result, the dysregulation of apoptosis can lead to a host of diseases including cancer and neurodegenerative disorders, establishing the importance of programmed cell death in the regulation of human health (1, 2).

The mitochondrially gated apoptotic pathway, known as intrinsic apoptosis, is initiated by a non-receptor-mediated stimulus, such as DNA damage or hypoxia (5). This stimulus generates an intracellular signal, leading to the opening of the mitochondrial permeability transition pore that results in a loss of mitochondrial membrane potential and subsequent release of a host of proapoptotic proteins into the cytosol. One of these, cytochrome c (CytC), catalyzes the formation of a large complex involving Apaf-1 (apoptotic protease-activating factor 1, henceforth Apaf1), known as the apoptosome (6, 7). Central to the regulation of intrinsic apoptosis is the interaction between the apoptosome and a protease called caspase-9 (Casp9) (7). In the absence of the apoptosome, Casp9 exists freely in the cytosol as an inactive monomer, but binding to the apoptosome leads to Casp9 activation, which subsequently activates caspase-3 (Casp3) and Casp7 via proteolytic cleavage, ultimately driving cell death (Fig. 1*A*) (8–10). Casp9 is part of the **c**ysteine-**asp**artic prote**ase** (caspase) family (11) and, like all members of this family, contains a Cys-His catalytic dyad to cleave target sequences immediately after an Asp (or in some cases Glu) residue (12–14). Casp9 is referred to as an initiator caspase, as its activation initiates caspase-mediated cell death, and its protease activity has only been observed upon dimerization (9, 15).

At the molecular level, Casp9 is a 416-residue enzyme that contains two functional domains. The N-terminal CAspase Recruitment Domain (CARD, residues 1 to 92) recruits Casp9 to the apoptosome by binding to the CARD of Apaf1, and the C-terminal Protease Domain (PD, residues 139 to 416) exhibits peptidase activity (Fig. 1*B*). A long,

Significance

Controlled cell death is critical for the well-being of multicellular organisms, with as many as 100 billion cells eliminated each day in an adult human. This process depends on the activation of the caspase-9 protease through binding to a large scaffold called the apoptosome. Once activated, caspase-9 activates downstream effector caspases that then degrade critical proteins, culminating in cell death. Here, we use NMR spectroscopy and biochemical assays to better understand the activation of caspase-9 molecules upon binding to the apoptosome. Our data challenge existing models of activation and establish that the apoptosome primes bound caspase-9 molecules for activation via dimerization that only occurs in the presence of substrate.

Author contributions: T.R.A. conceived the project; A.I.M.S., T.R.A., E.R., and L.E.K. designed research; A.I.M.S., T.R.A., E.R., Z.H.L., and L.E.K. performed research; A.I.M.S., T.R.A., E.R., J.M.A., Z.H.L., R.W.H., and L.E.K. analyzed data; A.I.M.S., E.R., J.M.A., Z.H.L., R.W.H., and L.E.K. discussed results and edited the paper; and A.I.M.S., T.R.A., E.R., and L.E.K. wrote the paper.

The authors declare no competing interest.

This article is a PNAS Direct Submission.

[1] A.I.M.S. and T.R.A. contributed equally to this work.

[2] To whom correspondence may be addressed. Email: reid.alderson@utoronto.ca, enrico.rennella@utoronto.ca, or lewis.kay@utoronto.ca.

This article contains supporting information online at https://www.pnas.org/lookup/suppl/doi:10.1073/pnas.2310944120/-/DCSupplemental.

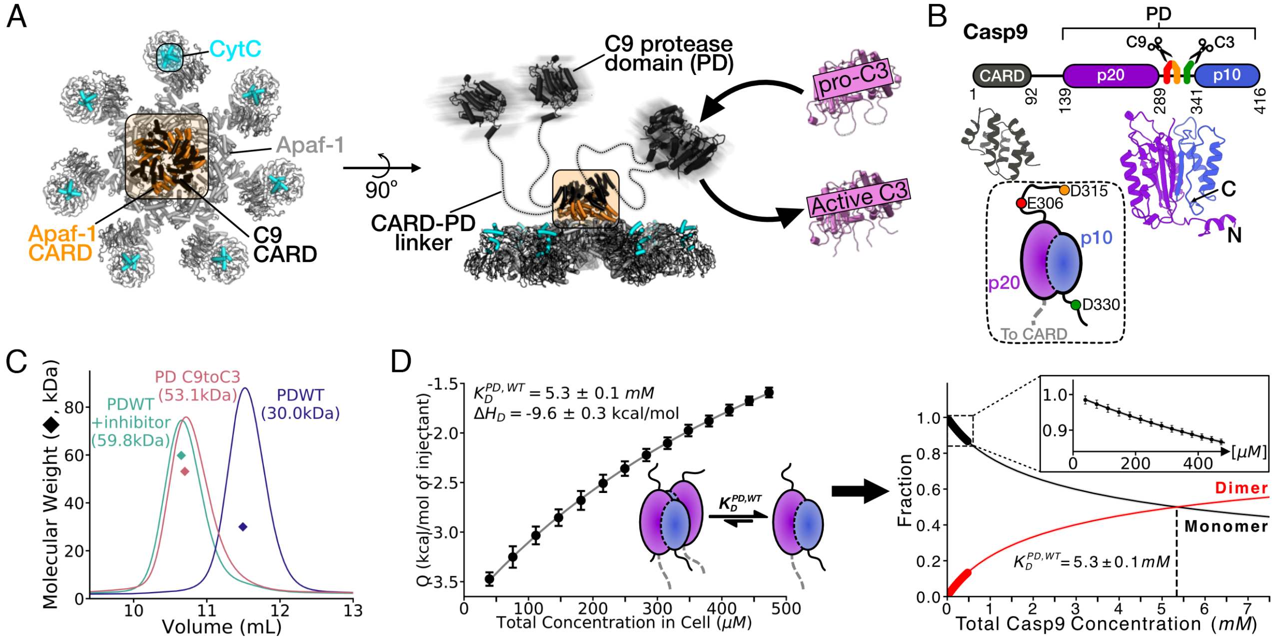

Fig. 1. The Casp9 (C9) PD is a monomer in solution. (*A*) End-on view of the apoptosome, a heptameric structure comprising seven copies of Apaf1 protomers and CytC (turquoise) that binds to the regulatory domain of each Apaf1 [*Left*, PDB ID: 5WVE (16)]. The $\text{CARD}_{\text{Casp9}}$ (black) and $\text{CARD}_{\text{Apaf1}}$ (orange) domains that anchor Casp9 to the scaffold are indicated by the box. Also shown is a view that is rotated by 90° highlighting the protease domains (PDs, either monomeric in the absence of substrate or dimeric upon interaction with substrate) [PDB ID: 1JXQ (9)] that activate the effector Casp3 (pink) [*Right*; PDB ID: 1QX3 (17)] via cleavage to promote cell death. (*B*) Domain organization of Casp9 (*Top*) and corresponding AlphaFold2 (18, 19) structures of these domains with linkers removed (*Bottom*); numbering highlights the start and end of the folded domains. The two Casp9 cleavage sites (red and orange) and a Casp3 cleavage site (green) in the linker connecting p20 and p10 of the Casp9 PD are shown. A cartoon representation of the Casp9 PD, used subsequently, with a cleaved p20-p10 linker at D315, along with cut-sites represented by colored circles is highlighted in the dotted box. (*C*) SEC-MALS profiles of WT Casp9 PD in the absence (navy) and presence (turquoise) of the substrate mimic "inhibitor" Z-LEHD-fmk and C9toC3 Casp9 PD (pink) are displayed. The experimentally derived molecular weights are in brackets and illustrated on the plot as diamonds. SEC profiles for FL Casp9 are shown in *SI Appendix*, Fig. S1. (*D*) ITC dilution experiments were fitted (solid line) using a dimer–monomer dissociation model (*Left*), and fraction monomer, $Frac_M$, (black circles), and dimer, $Frac_D$, (red circles) profiles were extracted (*Right*), as described in *SI Appendix*. Due to the very weak dimerization affinity ($K_D^{PD,WT}$ ~ 5 mM), only a small portion of the profile could be measured. The χ^2 error surface is shown in *SI Appendix*, Fig. S2. The fit was extrapolated and the total protein concentration at the point where $Frac_M = Frac_D$, corresponding to $K_D^{PD,WT}$, is indicated by the vertical dashed line (*Right*).

disordered linker (residues 93 to 138) separates the CARD from the PD (9, 20). The PD can be further subdivided into two subdomains: p20 (residues 139 to 289) and p10 (residues 341 to 416), which are connected by another long, disordered linker (residues 290 to 340). The p20-p10 linker contains two Casp9 recognition motifs that end in Asp/Glu (E306, D315) where autoproteolysis can occur. Prior to activation by the apoptosome, the cytosolic Casp9 polypeptide remains intact and is commonly referred to as proCasp9 (11, 21). Upon recruitment to the apoptosome, proCasp9 autocleaves to generate mature Casp9 (21), a process shown to be important for Casp9 activation when bound to the apoptosome (14) and implicated in additional regulatory pathways, such as the binding of X-linked inhibitor of apoptosis protein (XIAP) (22). A third site in the p20-p10 linker (D330) acts as a recognition motif for Casp3 cleavage that plays a role in the regulation of XIAP binding (14).

In contrast to Casp9, the apoptosome is a homoheptamer, composed of seven copies of the Apaf1 protein (16, 23, 24). Each Apaf1 monomer consists of a CARD (Fig. 1*A*—orange), an adenosine triphosphate (ATP) binding domain, and a regulatory domain that binds CytC (Fig. 1*A*—cyan). Prior to mitochondrial rupturing, the Apaf1 protein exists in the cytosol as a monomer, and only via interaction with the released CytC and ATP does it undergo a conformational change to allow formation of the heptameric apoptosome (Fig. 1*A*) (6, 25). This mechanism ensures that apoptosis is not inappropriately activated, thereby preventing unwanted cell death.

Recent cryoelectron microscopy (cryo-EM) structures of the heptameric apoptosome platform with bound Casp9 have revealed a detailed, albeit static picture of the assembled apoptosome (16, 26) (Fig. 1*A*). Notably, a single Casp9 CARD interacts with multiple Apaf1 CARDs via asymmetric interfaces with a 4:7 (Casp9:Apaf1) stoichiometry per apoptosome scaffold (27). While the $\text{CARD}_{\text{Casp9}}$-$\text{CARD}_{\text{Apaf1}}$ interactions, as well as the apoptosome platform itself, are well resolved in the cryo-EM structures, the Casp9 PDs are not observed, presumably because they are flexibly tethered to the apoptosome via long, disordered linkers (16). The flexibility of the Casp9 PDs has, thus far, prevented a detailed structural understanding of how PDs from multiple copies of the enzyme interact with each other while engaged with a single apoptosome scaffold. There is, therefore, considerable debate regarding the mechanism by which Casp9 activation occurs (16, 26–31). One hypothesis is that the recruitment of Casp9 to the apoptosome increases the local concentration of Casp9 monomers, leading to higher activity via increased PD homodimerization. An alternative proposal is that the dramatic increase in activity of apoptosome-bound Casp9 is due to a direct interaction between Casp9 PDs and unspecified regions of the apoptosome.

Solution-state NMR spectroscopy can often provide detailed insights into important motions and structural features that are necessary for function (32). This is the case even for flexibly tethered proteins and very high molecular weight particles, such as the apoptosome-Casp9 system considered here, where the aggregate molecular weight of the complex is 1.3 MDa. The combined use of highly deuterated molecules with $^{13}CH_3$-labeled methyl groups and NMR experiments that exploit a methyl transverse relaxation-optimized spectroscopy (TROSY) effect (33, 34) provides an opportunity for studies of a wide range of large complexes that are otherwise intractable to NMR.

Here, we use methyl-TROSY NMR, in combination with fluorescent substrate activity assays, isothermal titration calorimetry, and protein engineering, to inform on the mechanism by which Casp9 is activated. Notably, our NMR study reveals that the PDs of apoptosome-bound Casp9 molecules do not appreciably homodimerize until the addition of substrate, which then activates the enzyme. In addition, using a heptameric form of the *Thermoplasma acidophilum* 20S proteasome as a scaffold, we engineered an apoptosome mimic and found that it yields similar levels of Casp9 activity stimulation as the native apoptosome reconstituted from insect cells. Together, our results provide strong evidence that Casp9 activation is driven by molecular crowding on the apoptosome platform, rather than specific interactions with the platform itself. Binding to the apoptosome scaffold primes Casp9 for activation by facilitating rapid and extensive dimerization only when substrate becomes available, providing another layer of control in the regulation of apoptosis.

Results

Substrate-Free Casp9 Is a Monomer in Solution. Prior to investigating the dimerization propensity of Casp9 when bound to the apoptosome, we first sought to establish the self-dimerization constant of the enzyme in the substrate-unbound state. Fig. 1*C* shows profiles from size-exclusion chromatography in tandem with multiangle light scattering (SEC-MALS). In the absence of substrate, the Casp9 PD elutes as a monomer (calculated MW of Casp9 PD = 30 kDa), as expected, indicating a very weak dimerization constant. Addition of a fluoromethyl ketone (fmk) derivatized tetrapeptide, Z-LEHD-fmk, which acts as a substrate mimic (35, 36), irreversibly inhibits Casp9 by trapping it in an active conformation, because the fmk group forms a covalent bond with the Casp9 active-site cysteine (C287). SEC-MALS, performed on the enzyme in the presence of excess substrate mimic established a dimeric structure with a molecular weight very close to that predicted for the dimer (60 kDa, Fig. 1*C*). Notably, a mutant of the Casp9 PD, C9toC3, where five residues at the Casp9 weak dimer interface are replaced with the corresponding residues from Casp3, which has previously been shown to form a strong dimer (16, 37), resulted in a SEC-MALS profile similar to that of the Casp9 PD upon binding Z-LEHD-fmk (Fig. 1*C*). Similar SEC experiments were performed on full-length (FL) Casp9, showing identical behaviour as seen in the experiments on the PD (*SI Appendix*, Fig. S1). Thus, both the isolated PD and full-length forms of Casp9 are predominantly monomeric in solution in the absence of substrate, in agreement with previous studies (16, 37, 38).

We next obtained a quantitative measure of the dimerization affinity of substrate-free Casp9 by performing isothermal calorimetry (ITC) dilution experiments in which the heat of dissociation was measured from the successive addition of aliquots of Casp9 PD to an ITC cell containing only buffer. A dissociation constant, $K_D^{PD,WT}$, of 5.3 ± 0.1 mM was obtained from a fit of the released heat from each aliquot to a dimer–monomer dissociation model (Fig. 1*D* and *SI Appendix*, Fig. S2 and *Text*), with a similar value for the FL Casp9 construct (15 ± 2 mM, *SI Appendix*, Fig. S2). As Casp9 exists in the eukaryotic cytosol at nanomolar concentrations [~77 nM in HEK293T cells, (39)], our ITC data establish that the enzyme is monomeric in the absence of the apoptosome and/or substrate under physiologically relevant conditions.

As a first step toward quantifying interactions between adjacent Casp9 molecules on an apoptosome scaffold, we next recorded NMR spectra of Casp9 PD without and with substrate mimic, exploiting the fact that NMR is well suited to characterize weak intermolecular contacts at atomic resolution. Due to the relatively large molecular weight of monomeric and dimeric Casp9 (47 kDa and 94 kDa, respectively), and given our ultimate goal of studying apoptosome-Casp9 complexes (molecular mass ~1.3 MDa), we prepared highly deuterated Casp9 samples with $^{13}CH_3$-labeling at Ile-δ1, Leu-δ, Val-γ, and Met-ε positions, where only one of the pair of isopropyl methyl groups of each Leu and Val is $^{13}CH_3$ labeled [referred to as U-^{2}H, ILVM-labeling herein (40)]. Exploiting the methyl-TROSY effect (33), high-quality two-dimensional (2D) heteronuclear ^{1}H-^{13}C multiple-quantum coherence (HMQC) spectra were obtained from these samples (Fig. 2*A*).

Methyl resonances from the PD of Casp9 were assigned via mutagenesis (44) and a 3D heteronuclear multiple-bond HMQC experiment (45), with some assignments verified by analysis of ^{13}C-edited NOESY spectra. Mutagenesis-directed assignments were hindered by the fact that many of the Leu and Val residues are densely packed with each other and with aromatic residues, so that mutation of a single residue leads, in some cases, to shifting of multiple peaks. Unfortunately, only small quantities of highly deuterated Casp9 constructs containing the PD could be produced (typically less than 100 μM Casp9 in a 5 mm NMR tube was obtained from a 1 L growth in D_2O M9 media) that were not sufficient for triple resonance assignment strategies. In contrast, a ^{13}C,^{15}N-labeled CARD+linker sample (residues 1 to 138) could be generated in much larger quantities, such that assignments of the ILVM residues in the CARD and linker of Casp9 were obtained using triple-resonance experiments (46). Despite limitations with methyl assignments in the PD, we have obtained a reasonable number of methyl assignments of FL Casp9 to enable detailed mechanistic studies (19/19 Ile, 56/98 Leu, 22/50 Val, 7/7 Met, where the numerator and denominator tabulate the number of assigned vs. the number of expected peaks for a given methyl containing amino acid type).

Next, we wondered if the Casp9 CARD and PD stably interact. Prior studies found that, even though the PD is separated from the CARD by a long ~45-residue linker, the Casp9 protease activity was significantly modified by removal of the CARD+linker residues (residues 1 to 138) (16, 38, 47). However, we find that 2D ^{1}H-^{13}C HMQC spectra of U-^{2}H, ILVM-labeled Casp9 PD and U-^{2}H, ILVM-labeled Casp9 CARD+linker overlay very well with spectra of similarly labeled FL Casp9 (*SI Appendix*, Fig. S3), with no chemical shift perturbations (CSPs) for any methyl peaks. These results are consistent with the absence of stable interactions between the CARD and PD. A lack of CARD/PD interactions is also observed upon dimerization in the presence of the Z-LEHD-fmk substrate-mimic (*SI Appendix*, Fig. S3). Regrettably, our data do not provide insight into why Casp9 proteolytic activity is modified upon removal of the CARD+linker (16, 38, 47), nor why the K_D values for dimerization of the PD (5.3 mM) and FL (15.2 mM; *SI Appendix*, Fig. S2) constructs are slightly different. However, our NMR data do suggest that any structural perturbation that contributes to the change in activity must be very subtle. Thus, in both the absence and presence of substrate, the Casp9 domains are effectively "beads-on-a-string". For this reason, we have used the PD in a number of NMR studies below, since there is less resonance overlap in the NMR spectra in comparison to the FL construct.

Having chemical shift assignments for many methyl probes in substrate-free Casp9, we next sought to obtain the corresponding peak assignments for the dimeric form of the enzyme. Fig. 2*B* shows a superposition of spectra recorded of a 5 μM sample of U-^{2}H, ILVM-labeled Casp9 PD alone (navy, multiple contours and labeled *M*) and in the presence of a 10-fold excess of the

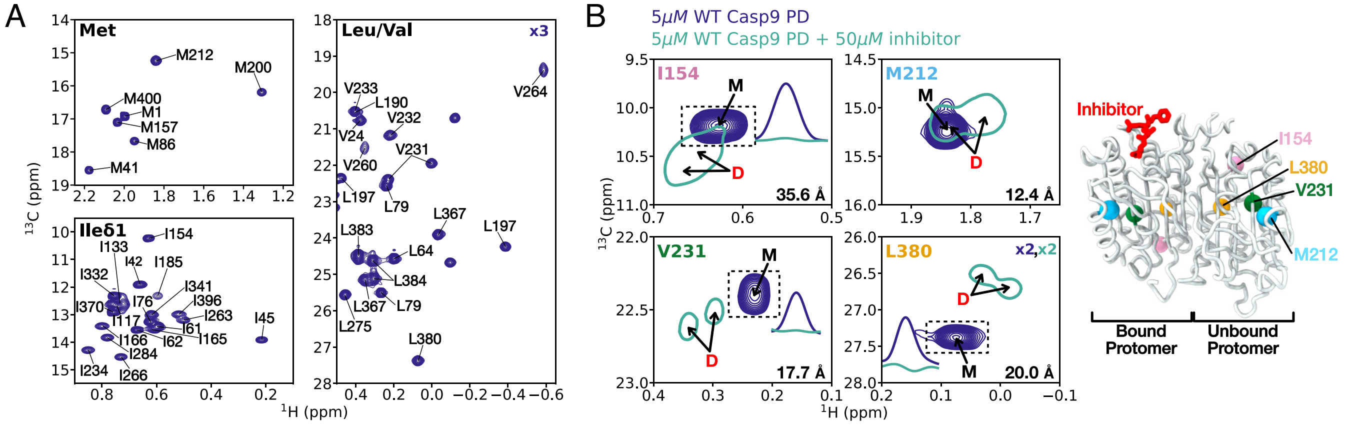

Fig. 2. Substrate binding shifts monomeric Casp9 PD to the dimeric form. (*A*) 2D ^{1}H-^{13}C HMQC spectrum of U-^{2}H, ILVM-labeled WT Casp9 recorded at 18.8 T (800 MHz, ^{1}H frequency) and 25 °C. Assignments of some of the cross-peaks are indicated. (*B*) (*Left*) Overlay of selected regions in 2D ^{1}H-^{13}C HMQC spectra of 5 μM U-^{2}H, ILVM-labeled WT Casp9 PD in the absence (navy contours) and presence (turquoise single contours) of the inhibitor (substrate mimic) Z-LEHD-fmk, 600 MHz, 25 °C. The methyl resonances from I154, M212, V231, and L380 are highlighted. One-dimensional ^{1}H traces adjacent to the monomer peaks for I154, V231, and L380 are "box-sums" (sums over the ^{13}C dimension) over the regions indicated by dashed boxes, corresponding to where the monomer cross-peaks are found (i.e., Casp9 PD in the absence of inhibitor), illustrating that for the PD:inhibitor concentration ratios used the monomer–dimer equilibrium is shifted completely to the dimer. For the L380 panel, contours start at a level twofold lower than for the other panels. (*Right*) The locations of the methyl groups in question are mapped onto a SWISS-MODEL (41–43) structure of the Casp9 PD dimer (*Right*), generated using a previously solved crystal structure with the inhibitor Z-EVD-Dcbmk [PDB ID: 1JXQ (9)]. In the presence of inhibitor, each selected methyl group gives rise to two unique peaks due to "half-of-the-sites" reactivity, where only one protomer is bound to inhibitor with the other remaining unbound. The distance between the carbon atom of each methyl probe and the closest inhibitor heteroatom, as measured in the SWISS-MODEL structure, is given in the *Bottom Right* of each panel (*Left*); for Leu and Val residues, the distance reported is that to the nearest methyl carbon of the two stereospecific isopropyl methyl groups.

Z-LEHD-fmk substrate mimic (turquoise, single contours and labeled *D*). At the 1:10 Casp9:inhibitor concentration used, all of the monomer peaks disappeared from the HMQC spectrum and were replaced by a second set of peaks that derive from the dimer (Fig. 2*B*, showing flat traces at the positions of the monomer peaks in the inhibitor bound state). Notably, a pair of dimer peaks was obtained for each of the methyl probes illustrated in Fig. 2*B*, with the doubling resulting from the inherent asymmetry of the Casp9 PD dimer, which exhibits "half-of-the-sites" reactivity (9, 28), in which only one of the two protomers binds substrate (Fig. 2 *B*, *Right*). In this manner, the magnetic environment of each of these probes is different between the two protomers of the dimer, and separate peaks are observed.

Chemical shift assignments of a subset of peaks in the dimeric state were obtained via mutagenesis, and four methyl-containing residues (I154, M212, V231, and L380; stereospecific assignments are not available for isopropyl methyl groups) with unique chemical shifts in the monomer and dimer states (Fig. 2*B*) have been used to study the monomer–dimer equilibrium in what follows. The positions of the four methyl probes have been mapped onto a SWISS-MODEL structure (41–43), based on the crystal structure of the inhibitor-bound PD [PDB ID: 1JXQ, (9)], with the distances between each methyl carbon and the nearest heavy atom of the inhibitor indicated in the *Bottom Right* of each panel (Fig. 2*B*). As the distances are always greater than 12 Å, and as large as 35 Å, the unique dimer chemical shifts of these methyl groups do not result from direct contacts with the inhibitor, but, rather, reflect structural rearrangements that occur upon dimerization. This is confirmed by spectra recorded on a mutant of Casp9 that shifts the monomer–dimer equilibrium partially to the dimeric state (see "*A Casp9 Mutant that Promotes Dimerization*"), where the positions of the dimer peaks are very similar to those observed in the Z-LEHD-fmk bound form of the enzyme.

A Casp9 Mutant that Promotes Dimerization. It is well known that mutation of the Casp9 active-site cysteine to an alanine (C287A Casp9; Fig. 3*A*) results in a catalytically null enzyme (10, 48). Notably, the NMR spectrum of a 340 μM U-^{2}H, ILVM-labeled C287A Casp9 PD sample in the absence of substrate showed multiple peaks for a number of methyl probes (Fig. 3 *B*, *Top*), and the intensities of these peaks either increased (dimer peaks) or decreased (monomer peaks) with increasing protein concentration, as illustrated for the I154, M212, V231, and L380 methyl groups in Fig. 3*B*. The monomer and dimer peaks for these residues in the C287A mutant could be readily assigned, as they shifted only a small amount from their corresponding positions in apo- and inhibitor-bound spectra of the WT PD, respectively (e.g., compare Fig. 3 *B*, *Top* with Fig. 2*B*).

The dimer dissociation constant, $K_D^{PD,C287A}$, for the C287A Casp9 PD was determined by performing a protein concentration titration, from 25 μM to 340 μM, monitored by a series of 2D ^{1}H-^{13}C HMQC datasets, which enabled quantification of the intensities of the monomer and dimer peaks at each point in the titration. As the rotational correlation times of the monomeric and dimeric forms of C287A Casp9 PD are different, it is expected that the decay rates of signals from monomers and dimers will also vary, potentially complicating the extraction of accurate measures of concentrations of each species from volumes of cross-peaks. With this in mind, ^{1}H relaxation rates were measured in cases where they could be reliably extracted (V231 and L380) and the volumes of peaks were corrected as described previously (49). As this led to only minor changes in volumes, which had little effect on the extracted equilibrium constants, we assumed that in cases of peak overlap (I154 and M212), where correction was not possible, that the volumes were robust measures of concentrations. For V231 and L380, where well-resolved monomer and dimer peaks were observed, both for C287A (Fig. 3*B*) and inhibitor-bound WT Casp9 (Fig. 2*B*), the fractions of monomer ($Frac_M$) and dimer ($Frac_D$) can be calculated simply as $Frac_M = \dfrac{M}{M + D1 + D2}$ and $Frac_D = 1 - Frac_M$, respectively, where M and $D1$, $D2$ are volumes of monomer and dimer peaks, respectively. However, in the cases of I154 and M212, one of the dimer peaks overlapped with the peak from the monomer (Figs. 2*B* and 3*B*), making it

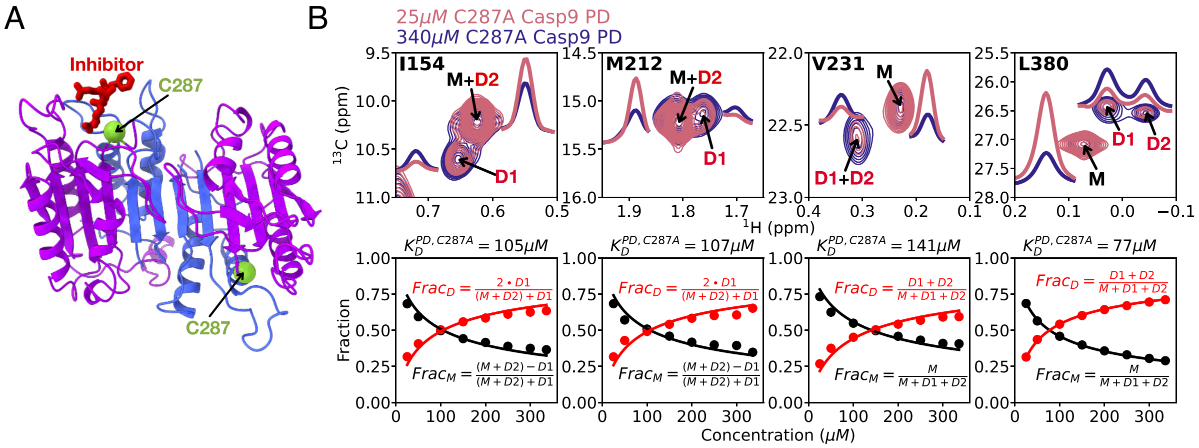

Fig. 3. The C287A mutation in the Casp9 PD increases dimerization affinity by 50-fold. (*A*) The location of the active-site cysteine (C287, green) is mapped onto the Casp9 PD dimer SWISS-MODEL structure. The bound inhibitor is shown in red. (*B*) Changes in relative peak volumes as a function of protein concentration are observed for monomer–dimer cross-peaks of selected residues in 2D ^{1}H-^{13}C HMQC spectra of U-^{2}H, ILVM-labeled C287A Casp9 PD (*Top*), 800 MHz, 25 °C. The 1D-traces of the box-sums for each cross-peak are shown adjacent to the peak in question and are summed over the following ^{13}C chemical shift ranges: I154 M+D2, 9.9 to 10.4 ppm; I154 D1, 10.5 to 11.0 ppm; M212 M+D2, 15.0 to 15.4 ppm; M212 D1, 14.9 to 15.3 ppm; V231 M, 22.2 to 22.6 ppm; V231 D1+D2, 22.4 to 22.8 ppm; L380 M, 26.9 to 27.4 ppm; L380 D1&D2, 26.2 to 26.7 ppm. The relative monomer population is greatest at 25 μM (pink contours) and decreases as the protein concentration increases to 340 μM (navy contours), with the opposite trend observed for the dimer population. For I154 and M212, one dimer peak (arbitrarily assigned as D2) overlaps with the monomer (M) correlation, while for V231 and L380, the two dimer peaks are distinct from the monomer peak. The fraction monomer (black circles) and dimer (red circles) as a function of concentration are plotted in the *Bottom* panels and fitted (solid lines) on a per residue basis, as described in *SI Appendix*, to extract the dissociation constants shown.

difficult to quantify $Frac_M$ and $Frac_D$ values directly from peak volumes. Assuming that both dimer peaks (*D1* and *D2*) have the same volume, an assumption that is shown to be accurate (*SI Appendix*, Fig. S4 and *Text*, "*Effect of assumption of equal volumes for I154 and M212 dimer peaks, D1 = D2*"), and assigning dimer peak 2 to be degenerate with the monomer peak, it then follows that $Frac_M = \dfrac{(M+D2)-D1}{(M+D2)+D1}$ and $Frac_D = \dfrac{2D1}{(M+D2)+D1}$. A monomer–dimer dissociation model was fit to the titration curves for each residue independently, with the corresponding $K_D^{PD,C287A}$ indicated above each panel in Fig. 3*B* (*SI Appendix*, *Text*). An average $K_D^{PD,C287A}$ of 108 ± 26 μM was obtained, where the error is the SD of the individual values. We have also estimated $K_D^{PD,C287A}$ based on an ITC dilution experiment of a C287A Casp9 PD sample (*SI Appendix*, *Text*), with a value of 270 ± 40 μM obtained, a difference of ~2.5 fold from the NMR results, corresponding to a $\Delta\Delta G$ of 0.5 kcal/mol (*SI Appendix*, Fig. S5). The small discrepancy between the measured $K_D^{PD,C287A}$ values likely derives from the fact that the NMR data were recorded on a deuterated sample in D_2O buffer in comparison with a protonated sample in H_2O for the ITC experiments (50). Our data, thus, establish a significantly higher dimerization affinity for C287A Casp9 relative to the WT protein.

What could account for the large difference in WT and C287A Casp9 K_D^{PD} values? We and others (9) observed that the addition of a covalent substrate mimic promotes dimerization when added to a WT sample of Casp9 (Fig. 2*B*). Because the C287A PD is catalytically inactive, the p20-p10 linker that contains the Casp9 cleavage sites at E306 and D315 remains intact, and binding of the linker–substrate to the active site could, thus, promote dimerization, much like Z-LEHD-fmk does. To test this hypothesis, we prepared a U-^{2}H, ILVM-labeled C287A Casp9 NMR sample where the two Casp9 autolytic sites, Thr^{301}-Ser-Pro-Glu-Asp-Glu^{306} and Ser^{310}-Asn-Pro-Glu-Pro-Asp^{315}, were both replaced with a TEV-protease cut-site (Glu-Asn-Leu-Tyr-Phe-Gln) (51). The sample was subsequently incubated with TEV protease, producing an inactive mutant with a cleaved p20-p10 linker, much like for the WT construct which is cleaved during protein expression in *Escherichia coli*, except for the C287A mutation. 2D ^{1}H-^{13}C HMQC spectra of p20-p10 linker-cleaved and uncleaved forms of the C287A Casp9 variant were very similar (*SI Appendix*, Fig. S6), with similar relative intensities of monomer and dimer peaks in each case. Thus, the increased dimerization affinity for C287A Casp9 is not due to binding of intact linker–substrate, but likely reflects small structural changes from the active-site mutation itself that propagate to the dimer interface. Indeed, a comparison of 2D ^{1}H-^{13}C HMQC spectra from ILVM-WT and -C287A PD monomers reveals a number of changes in chemical shifts (*SI Appendix*, Fig. S7), including from residues near the dimer interface (e.g., L384, V387, I396, M400). Given that these residues are up to 20 Å from the active site, we speculate that the C287A mutation remodels the active site pocket of Casp9 and allosterically alters the conformations of residues at distal sites within the PD. A structural connection between the active site and dimer interface is consistent with the known relation between substrate binding and dimerization in Casp9 and other initiator caspases (52–54).

A Proteasome-Based Apoptosome-Mimic. Our NMR and ITC results establish that the dimerization propensities of the PDs from both WT Casp9 and C287A Casp9 are weak, with no evidence of dimerization for the WT protein in NMR spectra. We hypothesized that binding to the apoptosome scaffold would shift the Casp9 monomer–dimer equilibrium to the dimer in the process of stimulating its proteolytic activity. Due to the large size of Apaf1 and its multidomain nature, properly folded FL Apaf1, at least in our hands, could only be produced from Sf9 insect cells, with the addition of excess CytC and ATP required to reconstitute the (fully protonated) apoptosome (16, 26). Only relatively small amounts of scaffold were generated in this manner, typically ~40 μM concentrations in 500 μL solution from 2.5 to 3 L of insect cells. Moreover, deuteration of insect cell-derived Apaf1, which could significantly improve spectra of the bound Casp9, was not possible, thus restricting the types of NMR experiments that could be performed on samples of the >1-MDa complex (see "*The Apoptosome Primes Casp9 for Activation upon Substrate Binding*", below). Therefore, we searched for an "apoptosome-mimic" that could both be deuterated and produced at higher concentrations for NMR studies. Previously, a protein engineering approach was employed to generate apoptosome mimics in which the heptameric scaffolds GroES or ClpP were used as templates (27). In this approach, the Apaf1 CARD (residues 1 to 105) was engineered onto the N-terminal end of each of the seven GroES/ClpP protomers to form a stable heptameric ring in solution that presents Apaf1 CARDs for high-affinity Casp9 binding. Similar increases in the activity of Casp9 were reported for these artificial systems as for a truncated apoptosome construct composed of seven copies of Apaf1 residues 1 to 591 (27). Large elevations in the rate of substrate catalysis upon Casp9 binding could also be produced using DNA-based synthetic apoptosomes (28).

Here, we have taken a similar approach to that described for GroES and ClpP, focusing in our case on the heptameric proteasome core particle from *T. acidophilum*. This complex forms a cylindrical structure comprising four concentric rings, α_7-β_7-β_7-α_7, each of which, in turn, contains seven copies of a single α or β protein (44). Deletion of residues 97 to 103 from the native α-subunit produces a stable heptameric single-ring structure (α_7) (55), which can be expressed as a deuterated complex in an efficient and cost-effective manner for studies by NMR (44). In order to ensure a high-affinity, 1:1 interaction with Casp9, we replaced the N-terminal, highly flexible 13-residues of each α subunit (56) with a 16-residue linker from Apaf1 (G90 to G105) preceded by a 17-residue peptide from *Saccharomyces cerevisiae*, referred to as Ark1p [actin-regulating kinase 1 peptide; (57)] (*SI Appendix*, Table S1). Ark1p binds with a submicromolar affinity and in a 1:1 manner to the actin-binding protein (Abp1p) SH3 domain (58–60), also from *S. cerevisiae*. We have therefore replaced the CARD of Casp9 (first 95 residues) with the 62-residue Abp1p SH3 domain and mutated Casp9 linker residues 121 to 128 to GFEVKKS [from Dronc, the Casp9 homolog in *Drosophila melanogaster* (61)]. We also included an additional Pro-to-Phe mutation at residue 122, as the original Casp9 sequence (RPETPRP) is similar to the SH3 domain recognition motif in the Ark1p peptide and thus could potentially bind to the Abp1p-SH3 domain, weakening the intended interaction between the Casp9 and α domains. Fig. 4*A* illustrates the modified constructs of Casp9 and α, which will be referred to as Casp9′ and α′ in what follows, respectively. The engineered α'_7 particle, which forms spontaneously from α′ (55), appears, at least in some respects, to be an excellent apoptosome mimic, as illustrated in Fig. 4*B*. Here the structures of α_7 [green; PDB ID 2KU1 (56)] with the N terminus of each protomer, a mimic for the Ark1p peptide attached to the end of each α′, highlighted in orange, and the apoptosome [gray; PDB ID 5WVE (16)] with CARD domains (orange) are compared. Viewed from the top face that forms the Casp9 binding interface, the two homo-heptameric structures have similar diameters of approximately 120 Å (α'_7) and 155 Å (apoptosome). However, unlike the apoptosome whose binding stoichiometry is 4:7 (Casp9:Apaf1), Casp9′ can, in principle, bind to α′ in a 1:1 manner, as the ~45-residue linkers connecting the SH3 and p20-p10 domains should be sufficiently long to enable seven bound Casp9′ molecules (Fig. 4*C*).

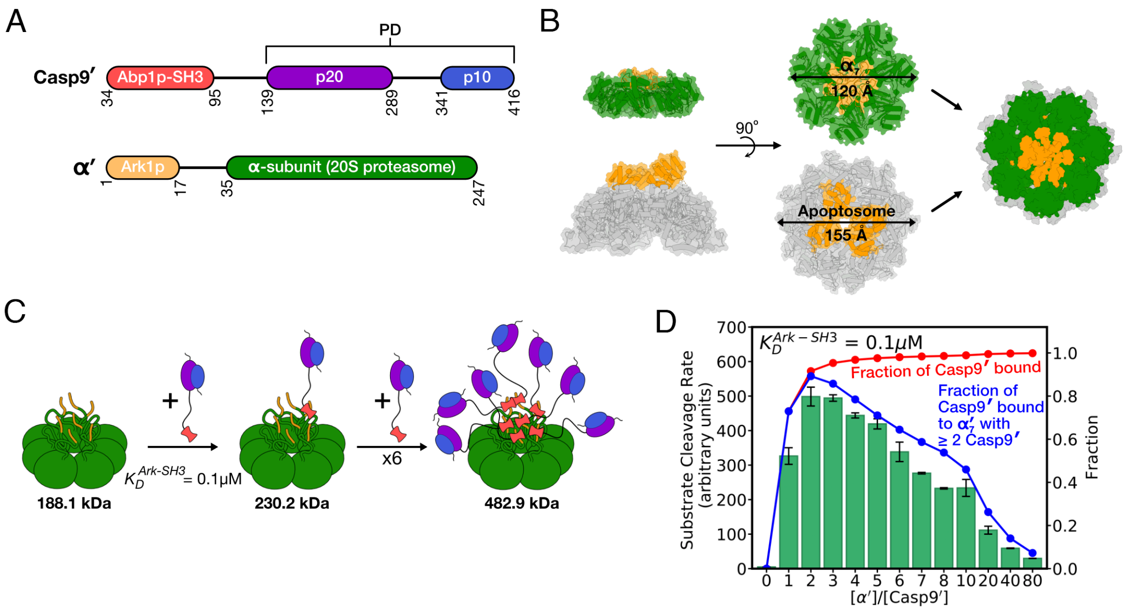

Fig. 4. A proteasome-based apoptosome mimic. (*A*) Domain organization of Casp9′ (*Top*) and α′ (*Bottom*). In Casp9′, the CARD is replaced by the Abp1p-SH3 domain, and numbering starts at residue 34 to keep numbering of the PD consistent with the WT Casp9 construct. In α′, the N-terminal gates of the α-subunit of the *T. acidophilum* 20S proteasome are replaced with an Ark1p peptide and an Apaf1 linker (see text for details). (*B*) Structural comparison of the α_7 ring [PDB ID: 2KU1 (56), green] and the apoptosome without the regulatory domains [PDB ID: 5WVE (16), gray], with the N-terminal gates (α_7) and CARDs (apoptosome) colored orange. The α_7 and truncated apoptosome rings are similar in diameter (compare middle structures), with the motifs responsible for binding Casp9′ (α'_7) and Casp9 (apoptosome) located in the regions colored orange in each molecule. (*C*) A schematic model of Casp9′ binding to α'_7. Unlike the apoptosome, which binds Casp9 molecules in a 4:7 ratio (27), the α'_7 scaffold can theoretically bind as many as seven Casp9′ molecules. The microscopic dissociation constant for each Casp9′-α′ interaction was determined to be 0.1 μM (*SI Appendix*, Fig. S8). (*D*) Plot of the cleavage rate of the fluorescent substrate peptide Ac-LEHD-AMC as a function of [α′]/[Casp9′], with [Casp9′] = 1 μM, and [α′] = 7[α'_7] varied between 0 and 80 μM (25 °C). Each measurement was performed in triplicate, and averages ± one SD (green bars) are displayed. The fractions of Casp9′ bound to α'_7 (red) and to an α'_7 scaffold with ≥2 Casp9′ molecules (blue) are illustrated, the latter rationalizing the observed activity profile.

We used ITC to measure the binding affinity of the Ark1p peptide and the Abp1p SH3 domain (*SI Appendix*, Fig. S8) under conditions that were subsequently used for α'_7-Casp9′ functional studies in order to ensure that binding of Casp9′ to the scaffold was nearly complete for the [α'_7]/[Casp9′] ratios used. The measured binding affinity, 0.13 ± 0.01 μM, establishes that this is the case, and, further, is consistent with the value measured using NMR on deuterated components at a lower pH [$K_D^{Ark-SH3}$ ~ 0.5 μM, pH 7.0 (58) vs. pH 8.0 used here], with the difference likely reflecting the fact that deuterated molecules were used in one measurement (NMR) and protonated in another (ITC). Fig. 4*D* shows the results of fluorescent activity assays quantifying the rate of cleavage of the fluorescent peptide Ac-LEHD-AMC (200 μM; AMC = Amino-4-methylcoumarin) by Casp9′ (1 μM) as a function of [α′]/[Casp9′]. Also shown is the fraction of Casp9′ molecules that are bound to α'_7 (red) assuming a model in which binding is described by a single microscopic dissociation constant (i.e., each binding event to the heptameric scaffold is independent), as well as the fraction of Casp9′ molecules bound to scaffolds containing at least two protease molecules (blue). The α'_7 -Casp9′ system exhibited an activity profile (green bars) that was dependent on scaffold concentration, whereby in the absence of α'_7 the Casp9′ cleavage rate was very low, but upon addition of α'_7 at a 1:1 concentration ratio of α′:Casp9′ the activity increased drastically, with a maximal level achieved for α′:Casp9′ of 2:1 to 3:1. However, upon further addition of α'_7, the activity dropped as the number of Casp9′ molecules per α'_7 scaffold decreased, consistent with an activity enhancement driven by molecular-crowding of Casp9′ PDs. A notable correlation between substrate cleavage rates and fraction of Casp9′ molecules bound to α'_7 containing at least two copies of protease is observed (Fig. 4*D*, green bars vs. blue curve) pointing to the importance of protein dimerization for the enhancement of activity, as is observed in Casp9 concentration dependent cleavage assays (*SI Appendix*, Fig S9). Notably, though, the activity assays of Fig. 4*D* do not inform on whether binding to the apoptosome is sufficient to induce Casp9′ dimerization or if, in addition, the presence of substrate is required.

Biochemical measurements, such as those illustrated in Fig. 4*D*, can provide insight into how stimulation of Casp9 activity might be achieved, but they are not a replacement for structural studies that ultimately can inform more deeply on the mechanism of activation. We recorded, therefore, a preliminary methyl-TROSY spectrum of an α'_7-Casp9′ complex prepared with an α′:Casp9′ ratio of 3:1 (240 μM U-^{2}H α′ and 80 μM U-^{2}H/ILVM Casp9′), focusing on the same four methyl group reporters of the PD monomer–dimer equilibrium that were discussed in a previous section ("*Substrate-Free Casp9 is a Monomer in Solution*"). Under these conditions, a maximum enhancement of Casp9′ activity is observed (Fig. 4*D*), indicating that many of the α'_7 particles have multiple bound proteases that would be required to form the dimeric structures needed for activation. Indeed, assuming a microscopic $K_D^{Ark-SH3}$ of 0.5 μM for the α′-Casp9′ interaction under the conditions of the NMR experiment of Fig. 5*A* where deuterated molecules are considered, approximately 74% of the scaffolds would have ≥2 bound Casp9′ molecules, 99.7% of Casp9′ proteases would be in the α'_7-bound state, and ~90% of Casp9′ ligands would be associated with α'_7 scaffolds with ≥2 bound Casp9′. Yet the positions of cross-peaks for all four methyl groups indicate that the PDs of the bound Casp9′ molecules are monomeric, with no evidence in support of any dimer formation (Fig. 5*A*).

The absence of any observable change to the PD monomer–dimer equilibrium upon WT Casp9′ binding to α'_7 is perhaps not unexpected given the very low degree of Casp9 self-association in the absence of scaffold (K_D values of 5 mM and 15 mM for the PD, Fig. 1*D*, and FL, *SI Appendix*, Fig. S2, WT Casp9 constructs, respectively). Consistent with this finding, additional NMR studies using a leucine-zipper linked dimeric form of Casp9 (Casp9 LZ) also establish that the WT PD of this construct remains monomeric (*SI Appendix*, Fig. S10*A*). We therefore produced U-^{2}H, ILVM-labeled C287A Casp9′ which has a much higher propensity to dimerize and for which a dimer dissociation constant of 213 ± 72 μM was measured (*SI Appendix*, Fig. S11) to establish whether in this case we could observe increased association of PDs from Casp9′ molecules bound to α'_7 due to molecular crowding. At an α′: C287A Casp9′ ratio of 2:1 (50 μM:25 μM), C287A Casp9′ is fully bound to α'_7, as observed in a comparison of 2D ^{1}H-^{13}C HMQC spectra of U-^{2}H, ILVM-labeled C287A Casp9′ in the presence and absence of U-^{2}H α'_7, focusing on peaks from the Casp9′ SH3 domain that shift upon binding to the Abp1p peptide component of α′ (Fig. 5*B*). We next recorded a titration series starting from a α′:C287A Casp9′ ratio of 2:1, to ensure that all C287A Casp9′ is fully bound, in which the concentration of α′ was increased from 50 μM to 250 μM, fixing the concentration of C287A Casp9′ at 25 μM so as to minimize the amount of dimerization in the absence of scaffold. Fig. 5 *C*, *Top* shows overlays of selected regions from the 2D ^{1}H-^{13}C HMQC spectra from the first (green) and last (blue) points in the titration, focusing on four methyl probes of the monomer–dimer equilibrium (I154, M212, V231 and L380), from which $Frac_M$ and $Frac_D$ values were quantified as before (black and red dots; see "*A Casp9 Mutant that Promotes Dimerization*"). Upon addition of the first aliquot of α'_7 to achieve an α′: C287A Casp9′ ratio of 2:1, all Casp9′ associate with the scaffold (i.e., approximately 3 to 4 Casp9′ bound to a given α'_7) and $Frac_D$ increases, indicating that binding of the C287A mutant to the scaffold does indeed increase dimer association in comparison to the unbound molecules. $Frac_D$ then begins to decrease as the Casp9′ molecules become distributed between more scaffolds (i.e., as [α′] / [Casp9′] increases), thus diluting the PDs associated with a given α'_7. We have fit a simple binding model to the $Frac_M$ and $Frac_D$ curves as a function of the concentration of added α′ (solid curves; *SI Appendix*, Fig. S12*A*), in which binding to α'_7 proceeds in two steps. First, C287A Casp9′ binds to a given α′ ($K_D^{Ark-SH3}$ = 0.5 μM; note that the K_D value measured for the binding of deuterated molecules was used here, as opposed to the equilibrium constant measured with ITC on protonated components, *SI Appendix*, Fig. S8), followed by the association of PDs from pairs of Casp9′ molecules that are tethered to the same scaffold. The second binding event is described in terms of a single fitted unimolecular dissociation constant, $K_{D,uni}$ (*SI Appendix*). Simulations establish that extracted values of $K_{D,uni}$ are very little affected by uncertainties in $K_D^{Ark-SH3}$ so long as [Casp9′] ≫ $K_D^{Ark-SH3}$ (*SI Appendix*, Fig. S12 *B* and *C*) as is the case here ([Casp9′] = 25 μM); $K_{D,uni}$ from each per-residue fit are listed above the panels in Fig. 5 *C*, *Bottom*. Similarly to the α′-scaffold, a C287A Casp9 LZ construct was found to promote dimerization, when compared to a C287A Casp9 PD sample of equal concentration (*SI Appendix*, Fig. S10*B*).

The Apoptosome Primes Casp9 for Activation upon Substrate Binding. The α'_7 apoptosome mimic provides insight into how a scaffold might play a role in activating Casp9 molecules arranged on its surface, but it is, nevertheless, an artificial system. Thus, we next focused on studies of the apoptosome prepared from the assembly of

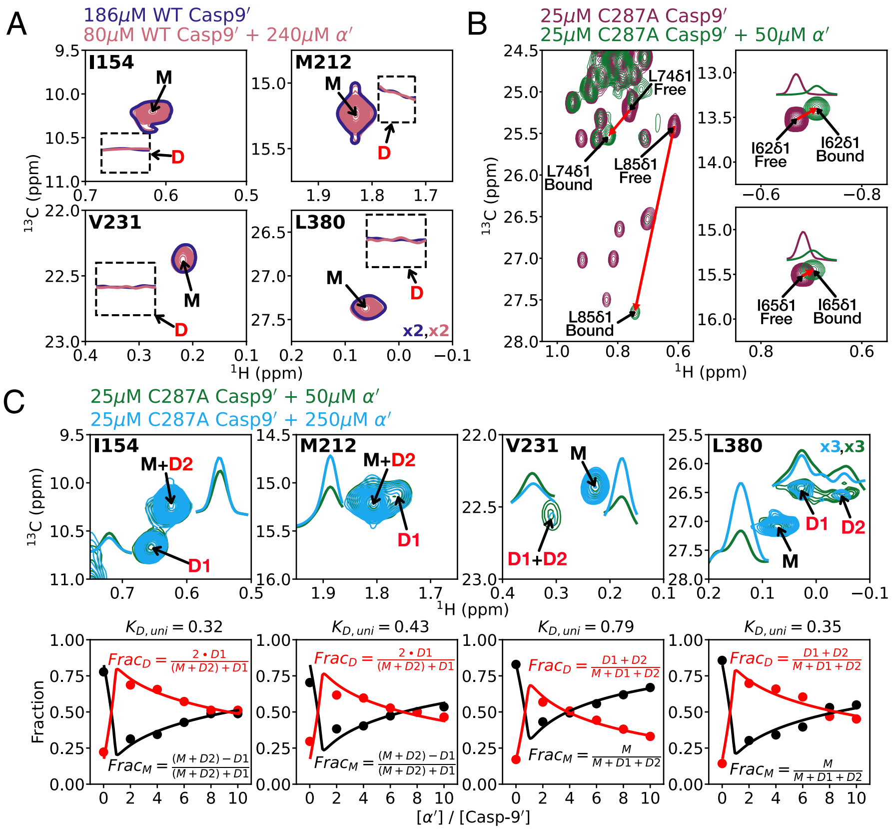

Fig. 5. Casp9′ remains monomeric when bound to the apoptosome mimic. (*A*) Superposition of selected regions of 2D ^{1}H-^{13}C HMQC spectra recorded on samples of 186 μM U-^{2}H, ILVM-labeled WT Casp9′ (navy single contour) and 80 μM U-^{2}H, ILVM-labeled WT Casp9′ + 240 μM U-^{2}H α′ (pink contours; [α′] = 7[α'_7]), 1 GHz, 25 °C, focusing on residues with distinct methyl-group chemical shift differences between monomeric and dimeric Casp9′. Only monomer (M) peaks are observed, with the expected positions of the dimer (D) peaks highlighted by dashed boxes, along with 1D box-sum traces, illustrating that dimer peaks are not observed. The 1D box-sum traces correspond to sums over regions within the boxes. (*B*) Selected regions of 2D ^{1}H-^{13}C HMQC spectra (800 MHz, 25 °C) highlighting Abp1p-SH3 methyl residues of 25 μM U-^{2}H, ILVM-labeled C287A Casp9′ in the absence (maroon contours) and presence (green contours) of 50 μM U-^{2}H α′. 1D box-sum traces establish that all methyl groups from Abp1p-SH3 residues at the binding interface with Casp9′ shift to their completely bound spectral positions at [α′]/[Casp9′] = 2 (for example, I62δ1, I65δ1, L74δ1, L85δ1), the lowest ratio used in titrations. (*C*) (*Top*) Superposition of selected regions of 2D ^{1}H-^{13}C HMQC spectra (800 MHz, 25 °C) focusing on monomer–dimer pairs for I154, M212, V231, and L380 (contours are plotted starting at a level threefold lower than for the other panels), recorded on samples of 25 μM U-^{2}H, ILVM-labeled C287A Casp9′ + 50 μM (green contours) or 250 μM (blue contours) U-^{2}H α′. The traces adjacent to the peaks are box-sums over the following ^{13}C chemical shift ranges: I154 M+D2, 9.9 to 10.4 ppm; I154 D1, 10.5 to 11.0 ppm; M212 M+D2, 15.0 to 15.4 ppm; V231 M, 22.2 to 22.6 ppm; V231 D1+D2, 22.4 to 22.8 ppm; L380 M, 26.9 to 27.4 ppm; L380 D1&D2, 26.2 to 26.7 ppm. These 1D box-sum traces highlight that monomer (dimer) peak volumes increase (decrease) for [α′]/[Casp9′] ≥ 2. (*Bottom*) $Frac_M$ and $Frac_D$ values (circles) as a function of the concentration of added α′ were fit to a binding model described in *SI Appendix* (solid curves) which was parameterized in terms of a bimolecular dissociation constant for the α′-Casp9′ interaction fixed to 0.5 μM and a residue-specific unimolecular dissociation constant, $K_{D,uni}$ (fitted value above each panel).

FL Apaf1 produced in insect cells and reconstituted via addition of excess CytC and ATP to form a 1.1-MDa complex (Fig. 6*A*). Unlike the truncated Apaf1 construct which lacks the regulatory domain that binds CytC, the FL apoptosome was stable at 25 °C for several days, so that NMR experiments could be performed on the native apoptosome-Casp9 system. Previous studies have determined that the apoptosome complex preferentially binds four Casp9 molecules via CARD$_{\text{Casp9}}$:CARD$_{\text{Apaf1}}$ interactions (Fig. 6*A*) (27), although more recent cryo-EM studies indicate that as many as five Casp9 molecules could be bound (16), with the first four localized to the central hub of the scaffold and the fifth to the periphery of the hub. Fluorescence activity assays using 1 μM Casp9 ± 1 to 8 μM apoptosome (Apaf1 concentration) and 200 μM of the Ac-LEHD-AMC fluorescent substrate demonstrate a drastic increase in substrate proteolysis by Casp9 upon addition of the apoptosome, with a maximal rate achieved at twofold excess of apoptosome monomer over Casp9 (Fig. 6*B*). This is then followed by a gradual decrease in activity as more scaffolds are added and a concomitant decrease in the numbers of bound Casp9 molecules below the optimum value of approximately four. A similar profile has been observed previously by Hu et al. using a truncated apoptosome construct (27).

As with the α'_7-Casp9′ complex, NMR can be used to establish whether Casp9 molecules tethered to the same apoptosome dimerize due to increased local concentration. However, the high molecular weight of the apoptosome-Casp9 complex (1.3 MDa, Fig. 6*A*), coupled with the fact that only protonated apoptosome could be prepared in Sf9 insect cells, challenges NMR studies of this system. Here, a modified ^{1}H-^{13}C methyl-TROSY approach is employed, using a truncated HMQC experiment in which detection of ^{1}H signal begins immediately after acquisition of ^{13}C chemical shifts, thereby eliminating a time-consuming element in the experiment during which signal decays (62). A sensitivity enhancement of well over twofold can be obtained for MDa complexes with this so-called "delayed decoupling" pulse sequence relative to the conventional HMQC experiment.

Fig. 6*C* highlights regions from ^{1}H-^{13}C methyl spectra recorded on samples of 20 μM U-^{2}H, ILVM-labeled FL WT Casp9 in the absence and presence of 45 μM unlabeled apoptosome (Apaf1 monomer concentration), at 25 °C. The 4:9 Casp9:Apaf1 ratio used to record the spectrum of the complex is slightly smaller than the 4:7 experimentally determined binding stoichiometry, ensuring that all added Casp9 molecules are bound. As the peaks in spectra

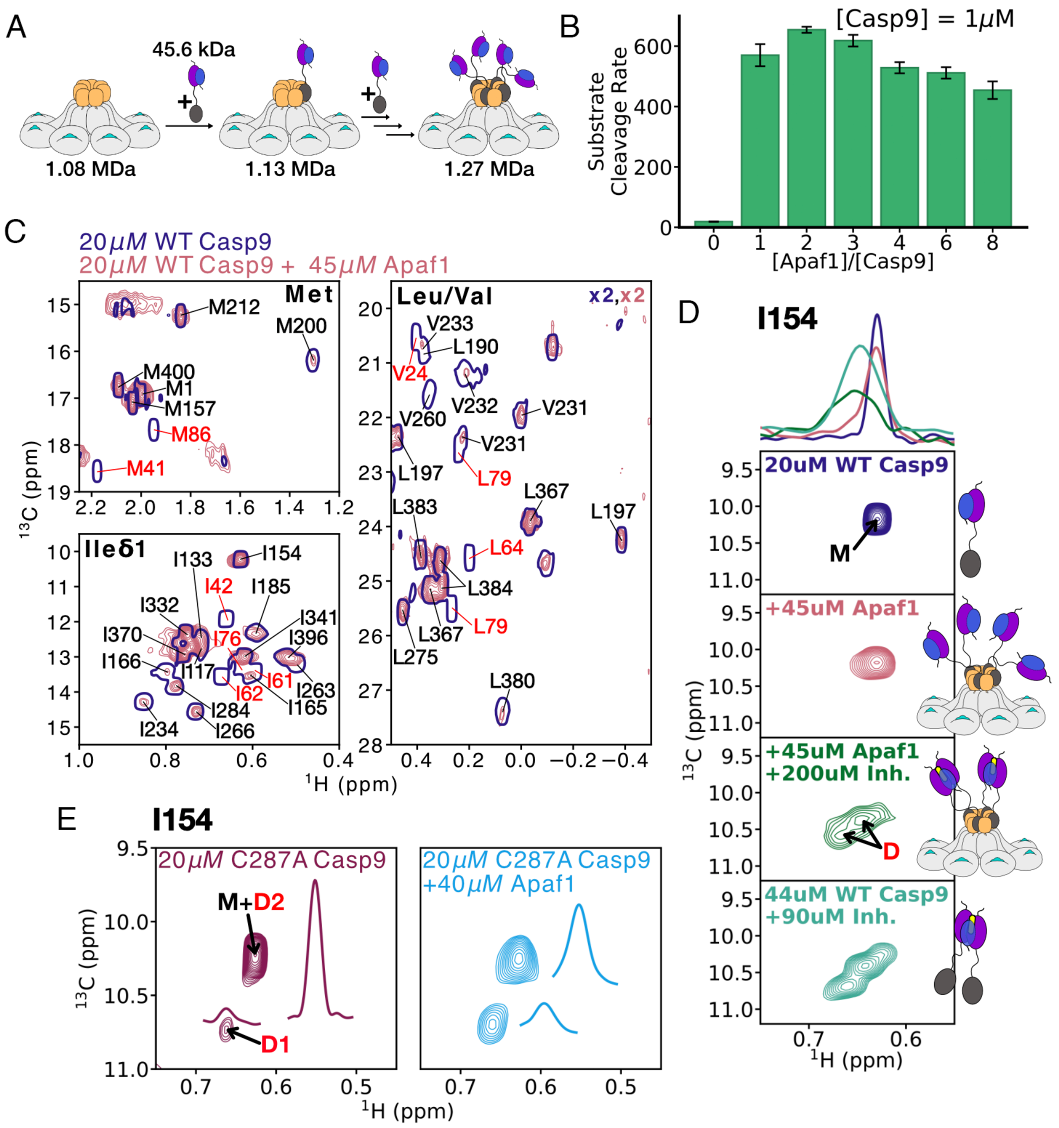

Fig. 6. Substrate induces dimerization of apoptosome-bound Casp9. (*A*) Schematic of Casp9 binding to the apoptosome in a 4:7 (Casp9:Apaf1) ratio. The coloring scheme of the components mirrors that of Fig. 1*A*. (*B*) Plot of the cleavage rate of fluorescent substrate peptide (Ac-LEHD-AMC) as a function of the [Apaf1]/[Casp9] ratio, where [Casp9] is fixed at 1 μM and [Apaf1] is varied between 0 and 8 μM, 25 °C. Triplicate measurements of each point were performed, and the average ± one SD is displayed. (*C*) Superposition of 2D delayed-decoupling ^{1}H-^{13}C HMQC spectra of 20 μM U-^{2}H, ILVM-labeled WT Casp9 in the absence (navy single contours) and presence of 45 μM Apaf1 (assembled apoptosome; unlabeled). Methyl cross-peaks derived from residues located in the Casp9 CARD (red assignment labels) disappear upon binding to the apoptosome due to rapid transverse relaxation caused by proximal protons in the fully protonated apoptosome. (*D*) Selected region of 2D delayed-decoupling ^{1}H-^{13}C HMQC datasets focusing on I154 of U-^{2}H, ILVM-labeled WT Casp9, 25 °C. In the absence of inhibitor, regardless of apoptosome binding, the Casp9 PD remains monomeric (*Top* two panels), and upon addition of inhibitor, the Casp9 PDs form homodimers (*Bottom* two panels). 1D ^{1}H "box-sum" traces are overlaid (*Top*). Shown on the right-hand sides of each plot are cartoons of the molecular species studied in each case. (*E*) Selected region of 2D delayed-decoupling ^{1}H-^{13}C HMQC spectra of 20 μM U-^{2}H, ILVM-labeled C287A Casp9 in the absence (*Left*, maroon contours) or presence of 40 μM (unlabeled) Apaf1 (right panel, blue contours). 1D ^{1}H traces (box-sum) are shown on top or to the right of the corresponding peak and correspond to sums over the following ^{13}C chemical shift ranges: I154 M+D2, 10.0 to 10.4 ppm; I154 D1, 10.6 to 11.0 ppm. All spectra were recorded on a 1-GHz NMR spectrometer, 25 °C, with the exception of the *Bottom* panel in *D* that was recorded at 800 MHz. Note that the concentrations of the monomeric building block of the apoptosome (Apaf1) are given throughout, but only the full heptameric apoptosome is actually present.

of free Casp9 are significantly more intense than those of the bound molecule, any free Casp9 would lead to disproportionately large signals in the NMR spectrum, and interpretation of these signals as arising from the bound conformation could result in erroneous conclusions. Our NMR data establish that all added Casp9 is bound. Very intense correlations from CARD$_{\mathrm{Casp9}}$ (residues 1 to 92) in spectra of the free Casp9 are completely absent in the bound state (assignments of CARD$_{\mathrm{Casp9}}$ peaks are in red, Fig. 6*C*), while other correlations that are much weaker in free Casp9 and that derive from the PD are observed in the complex. The absence of cross-peaks from CARD$_{\mathrm{Casp9}}$ in the presence of scaffold is due to the rapid decay of signal from methyl groups proximal to the fully protonated apoptosome, while the large distances between the apoptosome and PDs of bound Casp9 molecules ensure that many signals derived from the PD are still observed in the complex.

The strong correlation between peak positions in HMQC datasets of free and apoptosome-bound WT Casp9 (compare blue and pink peaks in Fig. 6*C*), coupled with the fact that free Casp9 is monomeric, provides strong evidence that the PDs of FL Casp9 do not homodimerize when tethered to the natural apoptosome. That this is the case can be established by focusing on I154 from Casp9, a residue whose δ1 methyl group has distinct monomer and dimer chemical shifts (Figs. 2*B* and 3*B*). Fig. 6*D* highlights that binding to the apoptosome does not change the position of the I154 δ1 peak (compare *Top* two panels), while addition of the inhibitor peptide Z-LEHD-fmk that has been shown to shift the Casp9 equilibrium completely to the homodimeric state (Figs. 1*C* and 2*B*) does so also in the apoptosome-Casp9 sample (compare *Bottom* two panels). Although the very weak dimerization of WT Casp9 molecules (K_D ~ 15 mM for Casp9 FL) biases against their association on the apoptosome (Fig. 6 *C* and *D*), we hypothesized that for C287A Casp9, for which a $K_D^{PD,C287A}$ value of approximately 110 μM was measured (Fig. 3*B*), the increased effective concentration of apoptosome-bound molecules would shift the monomer–dimer equilibrium to the dimer, as observed for C287A Casp9′ and α_7'. To test this hypothesis, we produced an NMR sample consisting of 20 μM U-^{2}H, ILVM-labeled C287A Casp9 with 40 μM unlabeled apoptosome monomer, with a slight stoichiometric excess of apoptosome over the experimentally determined 4:7 Casp9:Apaf1 ratio (27) to ensure that all molecules of C287A Casp9 were bound. Fig. 6*E* shows that the addition of the apoptosome to the C287A Casp9 sample increases the relative amount of dimer, as expected (compare *Left* and *Right* panels), due to a proximity affect in which Casp9 molecules are brought together by binding to the scaffold.

The increase in C287A Casp9 dimerization upon addition of the apoptosome can be quantified in terms of an effective total concentration of free C287A Casp9, $\left[\text{C287A Casp9}\right]_{eff}^{T}$ (i.e., not apoptosome bound) that would be required to achieve the same level of dimerization as observed when the enzyme is bound to scaffold. As described in *SI Appendix* (“*Estimating the effective concentration of C287A Casp9 bound to the apoptosome*”), $\left[\text{C287A Casp9}\right]_{eff}^{T}$ can be calculated from $K_D^{PD,C287A}$ and the $Frac_M$ or $Frac_D$ values obtained from volumes of I154 δ1 cross-peaks in the subspectrum highlighted in Fig. 6 *E*, *Right*. A value of $K_{D,uni} = 0.31$ is obtained (*SI Appendix*), along with $\left[\text{C287A Casp9}\right]_{eff}^{T}$ = 474 μM (monomer + dimer). We have also estimated what the local concentration of apoptosome-bound Casp9 is by calculating the volume that is available to four copies of the enzyme tethered to the central disk of the platform. These calculations started from the cryo-EM structure of the scaffold, which includes the CARD$_{\text{Casp9}}$:CARD$_{\text{Apaf1}}$ contacts (16) (*SI Appendix*). An accessible volume above the scaffold of approximately 1.18 × 10^{-20} L is calculated, from which a local concentration of tethered PDs of ~560 μM is obtained (*SI Appendix*, Fig. S13). Notably, the measured $\left[\text{C287A Casp9}\right]_{eff}^{T}$ and the calculated value for the local concentration of Casp9 bound to the apoptosome are similar.

Discussion

Apoptosis, the process by which many billions of unwanted cells in multicellular organisms are turned over each day, must be exquisitely controlled. This occurs, in part, by regulating a group of proteases, called caspases, whose activation initiates the final stages of cell death (2, 3, 5). In the case of the intrinsic apoptotic pathway, the binding of inactive Casp9 zymogen molecules to the heptameric apoptosome platform results in the self-cleavage of a long linker connecting two structured regions within the PD of the enzyme, contributing to the activation of apoptosome-tethered Casp9 molecules, which can then activate effector caspases, Casp3 and Casp7, via additional proteolysis events (6). Activated effector caspase molecules are then able to carry out cell death by proteolysis of essential cellular proteins such as those that play a structural role, are involved in the cell cycle, or are important for DNA metabolism (3, 5).

Significant advances have been made over the years in understanding how apoptosis is regulated at the molecular level via the proteolysis events described above. Cryo-EM images have delivered an atomic-resolution description of the apoptosome scaffold (16, 26, 63, 64), and cryo-EM and X-ray crystallography have identified the key interactions between CARD domains of the apoptosome and Casp9 that are responsible for formation of the apoptosome-Casp9 complex (16, 26, 27, 47), as well as providing significant clues as to how Casp9 activation is regulated. However, what remains critically lacking in these structural descriptions is information on the essential Casp9 PDs, as these are not observed in any of the images produced to date. Do PDs from neighbouring Casp9 molecules dimerize upon binding to a scaffold in the absence of substrate or only when substrate is present? Alternatively, do PDs interact with specific regions of the apoptosome which leads to activation?

Here, we have addressed these questions through methyl-TROSY-based solution NMR studies and activity assays with both native and engineered molecules. We have produced a mimic of the apoptosome-Casp9 system using a scaffold based on the α_7-rings from the *T. acidophilum* proteasome. CARD$_{\text{Casp9}}$:CARD$_{\text{Apaf1}}$ contacts that recruit Casp9 to the native platform have been replaced with interactions between an Ark1p peptide on α_7 and an Abp1p SH3 domain on Casp9, which bind each other with high affinity, so as to produce an α_7'-Casp9′ mimic whose activity profile can be measured and compared directly to that of apoptosome-Casp9. Figs. 4*D* and 6*B* show similar optimal substrate cleavage rates when using identical Casp9′ (Fig. 4*D*) and Casp9 (Fig. 6*B*) concentrations at a scaffold-monomer-to-protease ratio of 2:1. As α_7' shares no sequence homology, besides the linker between Ark1p and α_7, with the natural apoptosome, PD-scaffold interactions are not responsible for Casp9 activation, since similar levels of activity would then not be expected to be observed using the unrelated platforms. It is noteworthy that in previous studies using GroES- or ClpP-based apoptosome mimics, the scaffolds were generated by the addition of CARD$_{\text{Apaf1}}$ domains to each of the protomers of GroEL/ClpP and the activation of WT Casp9 tested (27). Unlike with α_7'-Casp9′ considered here, these experiments cannot rule out the possibility of CARD$_{\text{Apaf1}}$-Casp9 PD interactions playing a role in Casp9 activation. Finally, high levels of enhancement have also been observed using DNA-based origami versions of the apoptosome where CARD-PD contacts would also not be possible (28), again arguing against a major role for such interactions in the stimulation of Casp9 activity.

Our NMR spectra of Casp9′ in the α_7'-Casp9′ complex, and of Casp9 bound to the native apoptosome, show that in both cases, the Casp9 molecules remain monomeric (Figs. 5*A* and 6*D*). Proximity-driven dimerization does not appreciably occur in the apoptosome-Casp9 complex because the dissociation constant for WT Casp9 is high, with K_D values of ~5 mM, (*SI Appendix*, Fig. S2*A* and Fig. 1*D*), and ~15 mM, (*SI Appendix*, Fig. S2*B*) for the PD and FL constructs, respectively. The increase in effective Casp9 concentration in the complex is, therefore, not sufficient to cause a significant shift in the monomer–dimer equilibrium. In contrast, similar studies using C287A Casp9′ (Fig. 5*C*) and C287A Casp9 (Fig. 6*E*) show a clear shift toward increasing dimer population for both α_7'-Casp9′ and apoptosome-Casp9, respectively, as the K_D for the C287A Casp9 or Casp9′ monomer–dimer equilibrium is significantly lower (~100 to 200 μM). The observed shift in equilibrium upon scaffold binding implies that an effective concentration of the monomeric form of bound C287A Casp9 is on the order of the K_D or larger (or else there would be no observable change in the equilibrium). We estimate that a total concentration of free C287A Casp9 ($\left[\text{Casp9}\right]_{eff}^{T}$) of 474 μM would be needed to

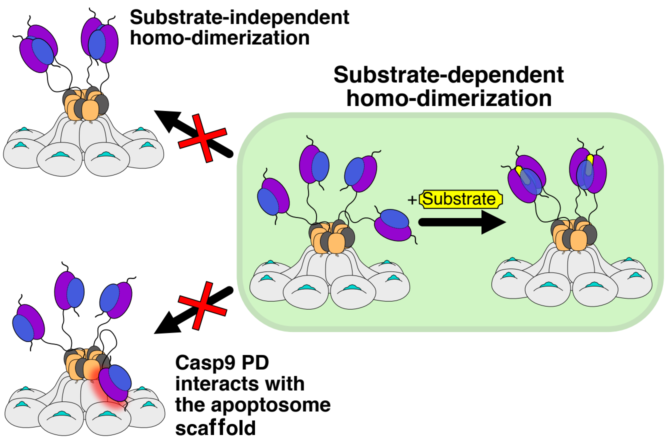

Fig. 7. Schematic of substrate-dependent Casp9 dimerization and activation on the apoptosome. PDs from Casp9 molecules that are tethered to the apoptosome remain largely monomeric in the absence of substrate but are poised to dimerize and activate upon substrate binding (*Right*, green box, with bound substrate shown in yellow). When Casp9 is bound to the apoptosome without substrate present, there is little proximity-induced dimerization of Casp9 PDs (*Upper Left*). Specific interactions between PDs and scaffold regions (*Lower Left*) do not appear to play a significant role, if any, in the activation process.

obtain the same level of dimerization as observed when the C287A Casp9 is bound to the apoptosome. Calculations of the volume accessible to Casp9 molecules on the surface of the apoptosome, starting from the cryo-EM model [PDB ID 5WVE, (16)], establish that the local concentration of four apoptosome-bound Casp9 molecules is on the order of 550 µM. Given that the concentration of Casp9 is reported to be 77 nM in HEK293T cells (39), the recruitment of Casp9 to the apoptosome enhances its local concentration by over 7,000-fold. In other enzymes, locally increased concentrations via the flexible tethering of catalytic domains by intrinsically disordered linkers have been shown to yield dramatic enhancements in the rate of catalysis, especially when the substrate concentration is low (65, 66). The effective concentration of a flexibly tethered catalytic domain depends on the length and conformational properties of the intrinsically disordered linker (67), and for Casp9, in particular, additional layers of complexity are provided by the stoichiometry when bound to the apoptosome, as well as the lifetime of the apoptosome-bound state.

The main results of our study are summarized in the schematic of Fig. 7, focusing on the Casp9 PDs that have been elusive to investigation by other structural methods. The weak dimerization affinity for the PD in the WT FL enzyme (K_D ~ 15 mM) prohibits a significant level of dimerization from occurring immediately upon formation of the apoptosome-Casp9 complex. For example, assuming an effective Casp9 concentration of ~500 µM on the apoptosome (*SI Appendix*, Fig. S13 and *Text*), and a K_D of 15 mM, approximately 5% of Casp9 molecules would be dimeric at any time. This could potentially facilitate stoichiometric autocleavage of the linker between the p20 and p10 domains of the PD that has been shown to be a necessary step in the activation of Casp9 (14), depending on the kinetics of cleavage relative to the lifetime of the dimer. In addition, the proximity of Casp9 molecules on the surface of the apoptosome would allow for their rapid and extensive dimerization as soon as substrate (i.e., Casp3) is available, as a further step in the activation process, as we have observed in NMR studies showing dimerization using a substrate mimic (Fig. 6*D*). The absence of a significant concentration of dimer without substrate may provide yet another level of protection by ensuring that a fully active complex only forms when needed. Our study of the 1.3-MDa apoptosome–Casp9 complex provides a compelling illustration of the synergy between cryo-EM and methyl-TROSY NMR, with detailed structural information about the well-defined apoptosome platform obtained through cryo-EM, supplemented by site-specific NMR data on the cryo-EM-invisible PDs. As critical domains of many high molecular weight complexes are often connected through flexible linkers, with nearly 60% of human proteins containing a mixture of structured domains and long IDRs (68), it is likely that a combined cryo-EM and NMR strategy will prove fruitful in studies of other systems, as well.

Data, Materials, and Software Availability. All study data are included in the article and/or *SI Appendix*.

ACKNOWLEDGMENTS. This research was funded by grants from the Canadian Institutes of Health Research (CIHR), FDN-503573 (L.E.K.), and the Natural Sciences and Engineering Research Council of Canada (2015-04347) (L.E.K.) and made use of the Biophysical Core Facility of the Hospital for Sick Children. We thank Prof. Yigong Shi and Dr. Yini Li (Tsinghua University) for insightful discussions regarding apoptosome expression and purification, Dr. Christopher Akey (Boston University) for providing the plasmid for Apaf1, and Dr. Hao Wu (Harvard University) for discussions about Casp9 activation. A.I.M.S. is grateful to the University of Toronto for an Ontario Graduate Scholarship. A.I.M.S. and Z.H.L. thank the Hospital for Sick Children Research Institute for Restracomp Graduate Scholarships. T.R.A. acknowledges financial support through a Banting Postdoctoral Fellowship (CIHR), and R.W.H. is supported by a Restracomp Fellowship from the Hospital for Sick Children Research Institute.

Author affiliations: [a]Department of Chemistry, University of Toronto, Toronto, ON M5S 3H6, Canada; [b]Program in Molecular Medicine, The Hospital for Sick Children Research Institute, Toronto, ON M5G 0A4, Canada; [c]Department of Molecular Genetics, University of Toronto, Toronto, ON M5S 1A8, Canada; and [d]Department of Biochemistry, University of Toronto, Toronto, ON M5S 1A8, Canada

1. C. B. Thompson, Apoptosis in the pathogenesis and treatment of disease. *Science* **267**, 1456–1462 (1995).
2. Z. Song, H. Steller, Death by design: Mechanism and control of apoptosis. *Trends Cell Biol.* **9**, M49–M52 (1999).
3. N. N. Danial, S. J. Korsmeyer, Cell death: Critical control points. *Cell* **116**, 205–219 (2004).
4. S. F. Gilbert, *Developmental Biology* (Sinauer Associates, ed. 6, 2000).
5. S. Elmore, Apoptosis: A review of programmed cell death. *Toxicol. Pathol.* **35**, 495–516 (2007).
6. H. Zou, W. J. Henzel, X. Liu, A. Lutschg, X. Wang, Apaf-1, a human protein homologous to C. elegans CED-4, participates in cytochrome c–dependent activation of caspase-3. *Cell* **90**, 405–413 (1997).
7. P. Li *et al.*, Cytochrome c and dATP-dependent formation of Apaf-1/caspase-9 complex initiates an apoptotic protease cascade. *Cell* **91**, 479–489 (1997).
8. M. Brentnall, L. Rodriguez-Menocal, R. L. De Guevara, E. Cepero, L. H. Boise, Caspase-9, caspase-3 and caspase-7 have distinct roles during intrinsic apoptosis. *BMC Cell Biol.* **14**, 32 (2013).
9. M. Renatus, H. R. Stennicke, F. L. Scott, R. C. Liddington, G. S. Salvesen, Dimer formation drives the activation of the cell death protease caspase 9. *Proc. Natl. Acad. Sci. U.S.A.* **98**, 14250–14255 (2001).
10. H. R. Stennicke *et al.*, Caspase-9 can be activated without proteolytic processing. *J. Biol. Chem.* **274**, 8359–8362 (1999).
11. E. S. Alnemri *et al.*, Human ICE/CED-3 protease nomenclature. *Cell* **87**, 171 (1996).
12. N. A. Thornberry *et al.*, A combinatorial approach defines specificities of members of the caspase family and granzyme B. *J. Biol. Chem.* **272**, 17907–17911 (1997).
13. L. E. Araya, I. V. Soni, J. A. Hardy, O. Julien, Deorphanizing caspase-3 and caspase-9 substrates in and out of apoptosis with deep substrate profiling. *ACS Chem. Biol.* **16**, 2280–2296 (2021).
14. Q. Hu, D. Wu, W. Chen, Z. Yan, Y. Shi, Proteolytic processing of the caspase-9 zymogen is required for apoptosome-mediated activation of caspase-9. *J. Biol. Chem.* **288**, 15142–15147 (2013).
15. K. M. Boatright *et al.*, A unified model for apical caspase activation. *Mol. Cell* **11**, 529–541 (2003).
16. Y. Li *et al.*, Mechanistic insights into caspase-9 activation by the structure of the apoptosome holoenzyme. *Proc. Natl. Acad. Sci. U.S.A.* **114**, 1542–1547 (2017).
17. C.-Z. Ni, C. Li, J. C. Wu, A. P. Spada, K. R. Ely, Conformational restrictions in the active site of unliganded human caspase-3. *J. Mol. Recognit.* **16**, 121–124 (2003).
18. M. Varadi *et al.*, AlphaFold protein structure database: Massively expanding the structural coverage of protein-sequence space with high-accuracy models. *Nucleic Acids Res.* **50**, D439–D444 (2022).
19. J. Jumper *et al.*, Highly accurate protein structure prediction with AlphaFold. *Nature* **596**, 583–589 (2021).
20. H. Qin *et al.*, Structural basis of procaspase-9 recruitment by the apoptotic protease-activating factor 1. *Nature* **399**, 549–557 (1999).
21. S. M. Srinivasula, M. Ahmad, T. Fernandes-Alnemri, E. S. Alnemri, Autoactivation of procaspase-9 by Apaf-1-mediated oligomerization. *Mol. Cell* **1**, 949–957 (1998).

22. J.-B. Denault, B. P. Eckelman, H. Shin, C. Pop, G. S. Salvesen, Caspase 3 attenuates XIAP (X-linked inhibitor of apoptosis protein)-mediated inhibition of caspase 9. *Biochem. J.* **405**, 11–19 (2007).
23. D. Acehan *et al.*, Three-dimensional structure of the apoptosome. *Mol. Cell* **9**, 423–432 (2002).
24. S. Yuan, C. W. Akey, Apoptosome structure, assembly, and procaspase activation. *Structure* **21**, 501–515 (2013).
25. S. J. Riedl, W. Li, Y. Chao, R. Schwarzenbacher, Y. Shi, Structure of the apoptotic protease-activating factor 1 bound to ADP. *Nature* **434**, 926–933 (2005).
26. T. C. Cheng, C. Hong, I. V. Akey, S. Yuan, C. W. Akey, A near atomic structure of the active human apoptosome. *Elife* **5**, e17755 (2016).
27. Q. Hu *et al.*, Molecular determinants of caspase-9 activation by the Apaf-1 apoptosome. *Proc. Natl. Acad. Sci. U.S.A.* **111**, 16254–16261 (2014).
28. B. J. H. M. Rosier *et al.*, Proximity-induced caspase-9 activation on a DNA origami-based synthetic apoptosome. *Nat. Catal.* **3**, 295–306 (2020).
29. C.-C. Wu *et al.*, The Apaf-1 apoptosome induces formation of caspase-9 homo- and heterodimers with distinct activities. *Nat. Commun.* **7**, 13565 (2016).
30. M. L. Würstle, M. Rehm, A systems biology analysis of apoptosome formation and apoptosis execution supports allosteric procaspase-9 activation. *J. Biol. Chem.* **289**, 26277–26289 (2014).
31. Y. Shi, Apoptosome: The cellular engine for the activation of caspase-9. *Structure* **10**, 285–288 (2002).
32. T. R. Alderson, L. E. Kay, NMR spectroscopy captures the essential role of dynamics in regulating biomolecular function. *Cell* **184**, 577–595 (2021).
33. V. Tugarinov, L. E. Kay, Ile, Leu, and Val methyl assignments of the 723-residue malate synthase G using a new labeling strategy and novel NMR methods. *J. Am. Chem. Soc.* **125**, 13868–13878 (2003).
34. J. E. Ollerenshaw, V. Tugarinov, L. E. Kay, Methyl TROSY: Explanation and experimental verification. *Magn. Reson. Chem.* **41**, 843–852 (2003).
35. B. A. Callus, D. L. Vaux, Caspase inhibitors: Viral, cellular and chemical. *Cell Death Differ.* **14**, 73–78 (2007).
36. N. A. Pereira, Z. Song, Some commonly used caspase substrates and inhibitors lack the specificity required to monitor individual caspase activity. *Biochem. Biophys. Res. Commun.* **377**, 873–877 (2008).
37. Y. Chao *et al.*, Engineering a dimeric caspase-9: A re-evaluation of the induced proximity model for caspase activation. *PLoS Biol.* **3**, e183 (2005).
38. K. L. Huber, B. P. Serrano, J. A. Hardy, Caspase-9 CARD: Core domain interactions require a properly formed active site. *Biochem. J.* **475**, 1177–1196 (2018).
39. N. H. Cho *et al.*, OpenCell: Endogenous tagging for the cartography of human cellular organization. *Science* **375**, eabi6983 (2022).
40. V. Tugarinov, L. E. Kay, An isotope labeling strategy for methyl TROSY spectroscopy. *J. Biomol. NMR* **28**, 165–172 (2004).
41. S. Bienert *et al.*, The SWISS-MODEL repository—New features and functionality. *Nucleic Acids Res.* **45**, D313–D319 (2017).
42. A. Waterhouse *et al.*, SWISS-MODEL: Homology modelling of protein structures and complexes. *Nucleic Acids Res.* **46**, W296–W303 (2018).
43. N. Guex, M. C. Peitsch, SWISS-MODEL and the Swiss-Pdb viewer: An environment for comparative protein modeling. *Electrophoresis* **18**, 2714–2723 (1997).
44. R. Sprangers, L. E. Kay, Quantitative dynamics and binding studies of the 20S proteasome by NMR. *Nature* **445**, 618–622 (2007).
45. L. Siemons, H. W. Mackenzie, V. K. Shukla, D. F. Hansen, Intra-residue methyl–methyl correlations for valine and leucine residues in large proteins from a 3D-HMBC-HMQC experiment. *J. Biomol. NMR* **73**, 749–757 (2019).
46. M. Sattler, C. Griesinger, J. Schleucher, Heteronuclear multidimensional NMR experiments for the structure determination of proteins in solution employing pulsed field gradients. *Prog. Nucl. Magn. Reson. Spectrosc.* **34**, 93–158 (1999).
47. E. N. Shiozaki, J. Chai, Y. Shi, Oligomerization and activation of caspase-9, induced by Apaf-1 CARD. *Proc. Natl. Acad. Sci. U.S.A.* **99**, 4197–4202 (2002).
48. H. Zou *et al.*, Regulation of the Apaf-1/caspase-9 apoptosome by caspase-3 and XIAP. *J. Biol. Chem.* **278**, 8091–8098 (2003).
49. R. Huang, F. Pérez, L. E. Kay, Probing the cooperativity of *Thermoplasma acidophilum* proteasome core particle gating by NMR spectroscopy. *Proc. Natl. Acad. Sci. U.S.A.* **114**, E9846–E9854 (2017).
50. P. J. Nichols *et al.*, Deuteration of nonexchangeable protons on proteins affects their thermal stability, side-chain dynamics, and hydrophobicity. *Protein Sci.* **29**, 1641–1654 (2020).
51. R. B. Kapust *et al.*, Tobacco etch virus protease: Mechanism of autolysis and rational design of stable mutants with wild-type catalytic proficiency. *Protein Eng. Des. Sel.* **14**, 993–1000 (2001).
52. N. Keller, M. G. Grütter, O. Zerbe, Studies of the molecular mechanism of caspase-8 activation by solution NMR. *Cell Death Differ.* **17**, 710–718 (2010).
53. N. Keller, J. Mares, O. Zerbe, M. G. Grütter, Structural and biochemical studies on procaspase-8: New insights on initiator caspase activation. *Struct. Lond. Engl.* **1993**, 438–448 (2009).
54. D. Datta, C. L. McClendon, M. P. Jacobson, J. A. Wells, Substrate and inhibitor-induced dimerization and cooperativity in caspase-1 but not caspase-3. *J. Biol. Chem.* **288**, 9971–9981 (2013).
55. R. Sprangers *et al.*, TROSY-based NMR evidence for a novel class of 20S proteasome inhibitors. *Biochemistry* **47**, 6727–6734 (2008).
56. T. L. Religa, R. Sprangers, L. E. Kay, Dynamic regulation of archaeal proteasome gate opening as studied by TROSY NMR. *Science* **328**, 98–102 (2010).
57. B. Fazi *et al.*, Unusual binding properties of the SH3 domain of the yeast actin-binding protein Abp1. *J. Biol. Chem.* **277**, 5290–5298 (2002).
58. P. Vallurupalli, D. F. Hansen, E. Stollar, E. Meirovitch, L. E. Kay, Measurement of bond vector orientations in invisible excited states of proteins. *Proc. Natl. Acad. Sci. U.S.A.* **104**, 18473–18477 (2007).
59. J. Haynes *et al.*, The biologically relevant targets and binding affinity requirements for the function of the yeast actin-binding protein 1 Src-homology 3 domain vary with genetic context. *Genetics* **176**, 193–208 (2007).
60. E. J. Stollar *et al.*, Structural, functional, and bioinformatic studies demonstrate the crucial role of an extended peptide binding site for the SH3 domain of yeast Abp1p. *J. Biol. Chem.* **284**, 26918–26927 (2009).
61. L. Dorstyn, P. A. Colussi, L. M. Quinn, H. Richardson, S. Kumar, DRONC, an ecdysone-inducible *Drosophila* caspase. *Proc. Natl. Acad. Sci. U.S.A.* **96**, 4307–4312 (1999).
62. N. Bolik-Coulon *et al.*, Less is more: A simple methyl-TROSY based pulse scheme offers improved sensitivity in applications to high molecular weight complexes. *J. Magn. Reson.* **346**, 107326 (2023).
63. S. Yuan, M. Topf, T. F. Reubold, S. Eschenburg, C. W. Akey, Changes in Apaf-1 conformation that drive apoptosome assembly. *Biochemistry* **52**, 2319–2327 (2013).
64. M. Zhou *et al.*, Atomic structure of the apoptosome: Mechanism of cytochrome c - and dATP-mediated activation of Apaf-1. *Genes Dev.* **29**, 2349–2361 (2015).
65. M. Dyla, N. S. González Foutel, D. E. Otzen, M. Kjaergaard, The optimal docking strength for reversibly tethered kinases. *Proc. Natl. Acad. Sci. U.S.A.* **119**, e2203098119 (2022).
66. M. Dyla, M. Kjaergaard, Intrinsically disordered linkers control tethered kinases via effective concentration. *Proc. Natl. Acad. Sci. U.S.A.* **117**, 21413–21419 (2020).
67. C. S. Sørensen, M. Kjaergaard, Effective concentrations enforced by intrinsically disordered linkers are governed by polymer physics. *Proc. Natl. Acad. Sci. U.S.A.* **116**, 23124–23131 (2019).
68. B. Tsang, I. Pritišanac, S. W. Scherer, A. M. Moses, J. D. Forman-Kay, Phase separation as a missing mechanism for interpretation of disease mutations. *Cell* **183**, 1742–1756 (2020).